Effect of precipitation kinetics on microstructure and properties of novel Al-Mn-Cr-Zr based alloys developed for powder bed fusion – laser beam

Journal of Alloys and Compounds 920 (2022) 165870

Contents lists available at ScienceDirect

Journal of Alloys and Compounds

journal homepage: www.elsevier.com/locate/jalcom

Effect of precipitation kinetics on microstructure and properties of novel Al-Mn-Cr-Zr based alloys developed for powder bed fusion – laser beam process

Bharat Mehta*, Karin Frisk, Lars Nyborg

Department of Industrial & Materials Science, Chalmers University of Technology, Göteborg, Sweden

ARTICLE INFO

Article history:
Received 9 March 2022
Received in revised form 16 May 2022
Accepted 11 June 2022
Available online 16 June 2022

Keywords:
Additive manufacturing
Powder bed fusion - laser beam
Aluminium-manganese alloys
Precipitation kinetics

ABSTRACT

This study investigates the precipitation kinetics and resulting effect on microstructure and property of a family of novel high strength Al-Mn-Cr-Zr alloys designed for powder bed fusion – laser beam process. The alloys have been shown to be printable without solidification cracking along with high supersaturation of solutes in as-printed state. Upon direct ageing, two families of precipitates namely Al-Mn and Al-Zr are observed. Al-Mn containing precipitates, which are observed in as-printed condition as nanometric precipitates decorating special regions are seen to grow preferentially at grain boundaries, which is followed by growth in bulk of the sample. A possible explanation is suggested to be a higher diffusivity at grain boundaries leading to faster growth while depleting solutes around grain boundary region quickly. The Al-Zr precipitation, which normally follows bulk precipitation is observed to co-precipitate with Al-Mn precipitates. Optimised heat treatments are seen to achieve peak hardness of 143 HV at 623 K for 24 h and 142 HV at 648 K for 14 h as compared to 102 HV in as-printed condition for one of the alloys. This overall hardening effect is attributed majorly to Al_3Zr nanoprecipitates along with semi-coherent $Al_{12}Mn$ precipitates.

1. Introduction

High performance aluminium (Al) alloys are used extensively in several mass-manufacturing applications in automotive and aerospace sector. Mostly, aluminium alloys are sought after owing to their high specific strength and attractive costs, which makes 2xxx, 6xxx and 7xxx series high strength aluminium alloys quite popular. These alloys gain most of their strength from age-hardening through tailored heat treatments [1,2]. Their specific strength in peak-aged condition is equivalent to that of quench and tempered carbon steel. The disadvantage of such alloys is their relatively lower service temperatures (< 473 K) [2–4]. With the advent of additive manufacturing (AM), new possibilities in terms of product design are made possible due to the layer-by-layer nature of the processing method. AM enables the possibility to build novel and complex geometries that cannot be realised with conventional manufacturing methods [5–7]. Initially used as a technology meant for rapid prototyping, AM is finding its way into serial manufacturing as more AM-specific designs are being developed, manufacturing technologies are becoming cost-efficient, and powder for manufacturing is becoming affordable. Powder bed fusion – laser beam (PBF-LB) is an AM technology where a laser beam of small spot size (40–100 µm diameter) is applied to selectively melt a layer of powdered material to build three-dimensional objects [5]. This method has been successfully used to reach near full densities (> 99.5%) and mechanical properties close or even superior to wrought materials [8–10].

The unique conditions in PBF-LB involving high local cooling rates constitute possibilities to create novel microstructures with expected gain in properties. The development of age-hardenable Al alloys tailored for PBF-LB has proportionally gained interest amongst researchers during recent years [11–16]. It has hence been demonstrated that the rapid melting and solidification achieved in PBF-LB processing allows for high supersaturation of solutes in the metal matrix beyond what is possible using conventional techniques, thus making it possible to alloy with a wider range of solutes with increased solubilities[17,18]. However, solidification cracking is still observed as a major hinderance when trying to qualify novel grades of Al-alloys. This occurs due to segregation of solutes in the melt and formation of low melting solutes such as Mg_2Si or Al-Fe-Si precipitates making it difficult to process such alloys [19]. Two effective

* Correspondence to: Postal address, Rännvägen 2 A, Göteborg 412 96, Sweden.
E-mail address: bharat.mehta@chalmers.se (B. Mehta).

https://doi.org/10.1016/j.jallcom.2022.165870
0925-8388/

solutions have been shown by researchers. By alloying with Sc/Si or by addition of TiB_2/ ZrH_2 [11,20,21], researchers have successfully shown to process these conventional alloys via providing nucleant phases such as Al_3Sc/ TiB_2 which act as a site for heterogenous nucleation of Al-grains, thus avoiding solidification cracking completely. Such alloys are later age-hardened using a T6-type conventional heat treatment or direct ageing heat treatment, dependent on the material or desired property [2,22]. A second method of avoiding cracking is via compositionally crack free materials [16,23] wherein the choice of solutes is done in a way that there is low solidification range combined with low amount of segregations close to solidification. Such a method thus created a family of "inherently crack free" materials as shown by the authors previously with good printability, limited in-process precipitation and tentative age-hardening response [24]. The family of alloys was Al-Mn-Cr-Zr based and was shown to contain large amount of solutes in as-printed condition (about three times the equilibrium solubility). Furthermore, the choice of solutes was done such that the age-hardening response should be at relatively higher temperatures (> 573 K) to expect thermal stability from these alloys, up to 523 K.

This study explores the next aspect of alloy design which is leveraging the high amount of solutes in the matrix to generate precipitation strengthening in a controlled manner via direct ageing heat treatments. Different heat treatments between 523 K and 678 K were tested and the ones with best ageing response were studied in further detail via advanced characterisation, X-ray diffraction and microhardness response. This was then studied together with thermodynamic simulations to see how well the precipitation behaviour is captured using simulation software.

2. Materials and methods

2.1. Powder

Pre-alloyed powder of different grades with spherical shape, fabricated by gas atomization process was provided by Höganäs AB, Sweden in standard particle size distribution of 20–53 µm. Table 1 summarises the chemical compositions of all alloys in as-atomised and as-printed condition based on ICP-AES values.

2.2. Modelling

All thermodynamic simulations were run using ThermoCalc 2021a software with TCAL7, MOBAL5 databases or with ThermoCalc 2019a using COST507 database [25]. This open database was used to assess the models for the precipitating phases, which are not available in commercial databases. The isothermal precipitation simulations were done with ThermoCalc 2021a software using PRISMA module. The alloy compositions for the simulation were assumed as the ones received from ICP-AES values, and it was supposed that all elements are dissolved in solid solution in as-printed state.

Table 1
Alloy composition for novel Al-Mn-Cr-Zr alloys. All compositions are in wt%.

Condition	Alloy name	Alloy composition (based on ICP-AES)
As-atomised	Alloy A	Al 4.7 Mn 0.48 Zr 0.15 Fe 0.16 Si
As-printed		Al 4.8 Mn 0.47 Zr 0.16 Fe 0.16 Si
As-atomised	Alloy B	Al 5.0 Mn 0.8 Cr 0.14 Fe 0.16 Si
As-printed		Al 4.9 Mn 0.8 Cr 0.18 Fe 0.17 Si
As-atomised	Alloy C	Al 5.0 Mn 0.8 Cr 0.59 Zr 0.16 Fe 0.16 Si
As-printed		Al 5.0 Mn 0.8 Cr 0.60 Zr 0.16 Fe 0.17 Si

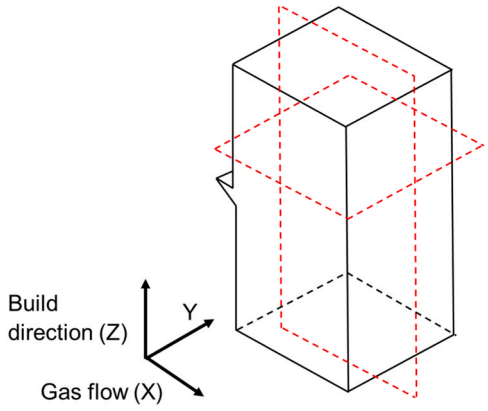

Fig. 1. Cuboidal design showing the cutting planes in red and the notch along to mark gas flow direction (Front plane: XZ; top plane: XY).

2.3. PBF-LB processing parameters and heat treatment

All alloys were processed in an EOS M100 machine with 40 µm spot size and 200 W (170 W nominal power) Yb-fiber laser. They were printed with 170 W power, 0.1 mm hatch distance, 1500 mm/s scan speed and 0.03 mm layer thickness with scan rotation of 67° between each layer. All the powder variants were exposed to drying at 353 K for 4 h before every print. The samples were printed as 8 mm x 8mmx 16 mm cuboids with a notch to mark direction of gas flow as shown in Fig. 1. After printing, the samples were cut with a cold saw from the build plate. Each sample which was heat treated was introduced into a pre-heated resistance furnace with a secondary thermocouple to verify the temperature close to the sample and to keep temperature control within ± 2 K, followed by quenching in water at room temperature (293 K). Heat treatment temperatures used for this study were between 523 and 678 K. Table 2 summarises the different heat treatments conducted on all five alloys.

2.4. Microstructure evaluation and hardness testing

The samples were cut close to the centre of XZ plane at about 3–4 mm from centre of top plane as shown in Fig. 1 followed by mounting in epoxy-based conductive thermoset resin. The samples were grinded with 200, 500, 800, 1000, 2000, 4000 grit silica foils followed by polishing with 1 µm diamond-based polish and a final step with OP-S silica suspension from Streurs on a Streurs TegraPol 31 machine. Some samples were etched using standard Keller's reagent for making precipitates or grain contrast visible for light optical microscopy. Light optical microscopy was done on a ZEISS Axioscope 7 machine with an automated scale enabling the stitching of images of large cross sections. Microstructural evaluation was also done using a Zeiss Gemini 450 SEM equipped with field emission gun source equipped with a six channel back scattered detector. Imaging was done with back scattered electron (BSE), in-lens and secondary electron (SE) receivers, depending on contrast and

Table 2
Summary of heat ageing cycles used for all Al-alloys.

Heat treatment	Temperature (K) and duration (hr) of ageing	Alloys used	Number of samples
1	648 K (0–10 hr), 678 K (0–10 hr)	A, B	32
2	523 K (0–24 hr), 573 K (0–10 hr), 598 K (0–10 hr), 623 K (0–24 hr), 648 K (0–24 hr, 100 hr), 678 K (0–10 hr)	C	49

resolution required. The SEM is fitted with a Bruker Quantax Flat-Quad Energy Dispersive X-ray Spectroscopy (EDX) detector, which enabled elemental mapping of microstructure at sub-micron resolutions. For these measurements, low beam voltage of 4 kV with 1 nA of probe current was chosen, in order to detect chemistries at nominal lateral resolutions as low as 0.15 µm. Each feature analysis scan was conducted at 4096 image resolution and detection limit of 6 pixels, thus detecting sub-micron features with detection limit kept at 0.15 µm. The software detects features based on different filters, in this case grey contrast from BSE detector which was manually adjusted to remove noise detected as features. In the feature analysis tool, acquisition mode was kept to 1.5 s of live time. This time was observed to be optimum to reduce the standard deviation of chemical composition for Mn-rich precipitates < 2 wt% and keep detection time of each scan less than 15 h, depending on how many precipitates were detected. The feature scanning function was used in Aztec v5.0 software from Oxford Instruments to detect, quantify and describe apparent chemistry of the nano-precipitates in the Zeiss Gemini 450 SEM machine. The foils for scanning-transmission electron microscopy (S-TEM) were prepared by following standard preparation technique to make a 0.12–0.14 mm foil along XZ direction followed by punching out 3 mm discs, which were electropolished with standard Streurs preparation for Al-alloys. The electropolishing was conducted on a Streurs TenuPol 5 machine with freshly prepared A2 electrolyte at + 1ºC, 35 V, 16 flow rate as settings. After TEM sample preparation, the samples were imaged using probe-corrected Titan 80–300 kV TEM with C2 aperture size of 70 µm and spot size 6. The X-ray diffraction (XRD) of samples was conducted at Höganäs AB on a finely grinded sample (2000 grit size) using a Bragg-Brentano HD X-ray machine with a Cu source (Kα = 1.5406 Å) with 40 mA and 45 kV as the generator settings, scanned between 20°– 100° 2Θ with a step size of 0.007° and scan step time of 1 s. The XRD patterns were analysed using DIFFRAC.SUITE EVA software from Bruker and the database used for pattern identification was PDF-4 + 2020 database. The Vickers hardness testing was done as per ASTM standards E92, E384 on all the samples. This was conducted using a DuraScan system (from Streurs) keeping a load of 0.3 kg, hold time of 10 s and spacing of at least five times the indentation dimensions. 16 points (4 ×4 grids) were taken along both front planes (XZ) and top plane (XY) of each sample and averaged to get range of hardness for each sample.

3. Results

3.1. Solidification simulations of the alloys in as-printed condition

The equilibrium phase evolution as function of temperature has been utilized as a tool for identification of possible phases that could result from PBF-LB processing. It was also used as an indication to stability of certain phases at higher temperatures, expected to be found during heat treatments. Example of such predicted phase evolution is shown in Fig. 2 for Alloy C. The Alloy C constitutes the most alloyed variant among the alloys tested in this study and consequently it is also the most important one to consider for the prediction of phase evolution. The equilibrium calculations shows that below 670 K, Al_6Mn is stable together with $Al_{12}Mn$. This also suggests that during heat treatment around such temperature after PBF-LB processing, both these precipitates could form from a supersaturated solid, and their possible equilibrium quantities would be varying significantly depending on small temperature differences.

These calculations are crucial to understand the starting point of PBF-LB processed materials and what types of phases could form upon ageing. Additionally, there could be minor elements such as Fe affecting the stabilities of Al-Mn precipitates which is illustrated in the supplementary section.

3.2. Direct ageing response

All the alloys were tested for direct ageing at different temperatures as mentioned in Table 2. This provided a comprehensive understanding of the hardening behaviour of the alloy systems with change in composition and temperatures. Alloy C was chosen as the alloy for several different temperatures between 523 K and 678 K and times between 0 and 24 h. As shown in Fig. 3a-b, the hardness response is quite temperature sensitive close to 670 K (as suggested before in Fig. 2); increase of only 30 K from 648 K to 678 K changes the time for ageing response significantly. As seen in Fig. 4, the hardening response at 648 K reaches up to 142 HV after 14 h, whereas it never crosses 130 HV at 678 K. The effect of combining Mn, Cr, Zr can be clearly seen by observing the hardening responses for alloy A (Mn,Zr alloyed), B (Mn,Cr alloyed) and C (Mn,Cr,Zr alloyed). It is observed in Fig. 3a) that alloy A and alloy B show 23% and 15% hardness increase respectively after ageing at 648 K, while having all three elements together in alloy C gives a 34% hardness increase. A similar effect is also visible when ageing at 678 K, where over-ageing starts after 6 h for alloys A and C whereas it starts after 2 h in alloy B. Fig. 4 shows that only temperatures > 573 K produce hardening response in alloy C. Alloy C was also tested for potential long term microstructural stability by heating at 648 K for 100 h and resulting hardness of 122 HV was observed (not shown in hardening curves). This suggests slow loss of hardness over longer time and possible high temperature stability. Ageing at 623 K and 648 K produced best hardening responses. At 623 K, it is observed that continuous hardening response up to 143 HV (40% hardness increase) is achieved in 24 h. At 648 K, there seems to be a double ageing response with an initial hardness increase to 136 HV after 8–10 h followed by secondary peak of 142 HV after 14 h thus showing about 40% hardening compared to the as-printed condition. The hardening response is attributed to Al-Mn and Al-Zr family of precipitates. This temperature of 648 K was thus chosen as the temperature of interest to analyse the microstructure-property correlation in more detail in forthcoming sections.

3.3. X-ray diffraction

X-ray diffraction (XRD) was conducted on samples from alloy C aged at 648 K and 678 K for selected times to investigate the changes in matrix composition on ageing. Estimation of amount (volume fraction) of precipitates by means of XRD was not pursued owing to factors such as texture in samples (during PBF-LB processing), low amount of precipitates (in as-printed condition) and overlap of minor peaks (particularly for $Al_{12}Mn$ and Al_6Mn phases). Fig. 5a) shows the peak shift observed for the major fcc-Al peak at 2Θ of around 45º for alloy C aged at 648 K for different times. Fig. 5b) shows the derived lattice parameter for the peak positions relative to pure Al. It is seen that lattice parameter value nominally equal to that of pure Al when ageing alloy C at 648 K and 678 K was reached after 24 h and 8 h respectively. This suggests as expected faster rate of solutes diffusing out of the matrix at higher temperatures. Fig. 5c)-d) presents the calculations using PRISMA module in ThermoCalc for the aforementioned temperatures; that about 25 h and 5 h are supposed to be needed to reach < 0.5 wt% of total solutes in the matrix. Consequently, there is a good fit between experimental observations and theoretical predictions.

Table 3 shows the crystallographic parameters expected for the phases of concern for the Al-Mn-Cr-Zr alloy family in as-printed and aged conditions. From Fig. 6a), considering alloy C, from the inset covering the range 38°– 45°, it is observed that minor peaks representing Al_6Mn and possibly $Al_{12}Mn$/ Al_3Zr occur in as-printed state. As seen in Fig. 2, the phase equilibria calculations indicate Al_6Mn as a possible phase and its presence is clear. The small peaks at around 2Θ of 41.3° may also correspond to $Al_{12}Mn$ or Al_3Zr phases.

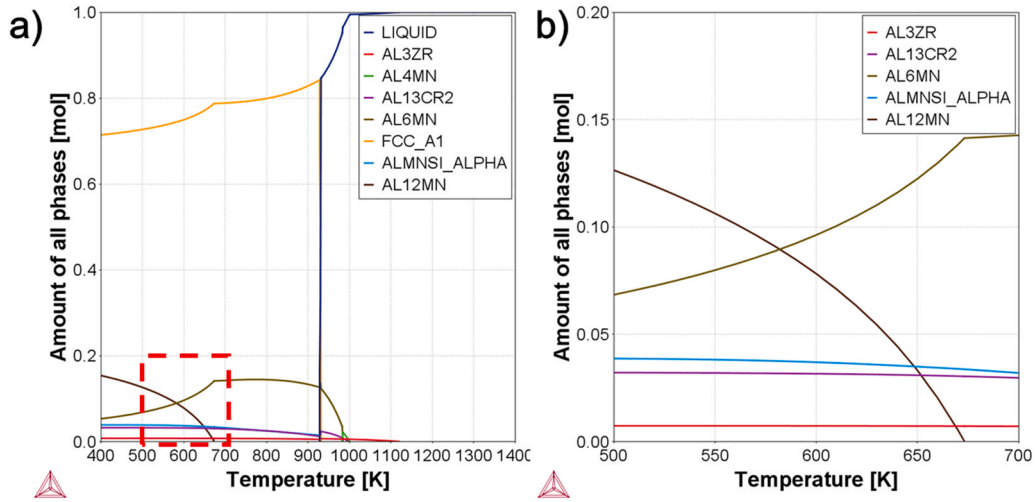

Fig. 2. a) One axis equilibrium simulation showing the stable precipitates and phases at varying temperatures of Alloy C and inset marked in red b) Zoomed in between 500 and 700 K and < 0.2 mol fraction of precipitates focusing on $Al_{12}Mn$ and Al_6Mn precipitates. Calculations done with COST507 database using ThermoCalc2019a [25].

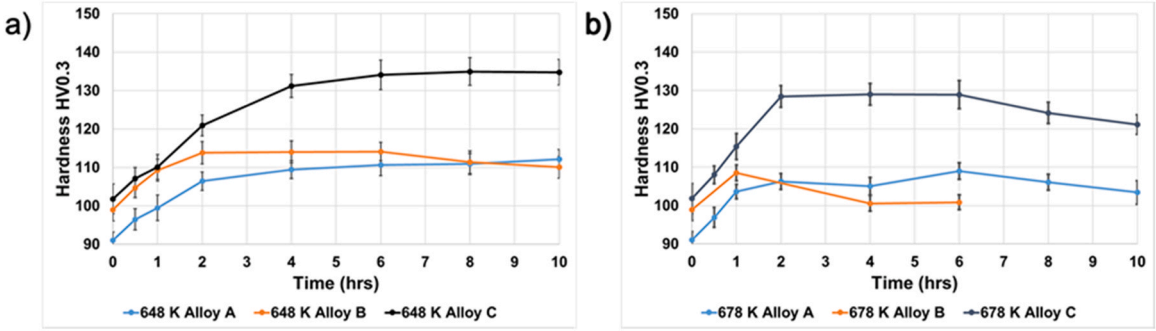

Fig. 3. Vickers hardness (HV0.3) test done on all alloys at a) 648 K and b) 678 K [24] between 0 and 10 h. Hardness data is averaged for XZ and XY directions and error bars of one standard deviation shown.

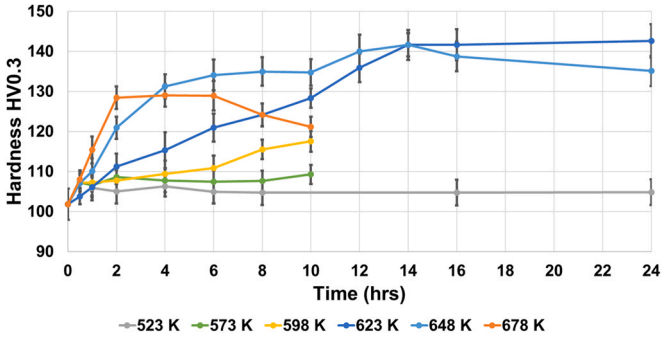

Fig. 4. Vickers hardness (HV0.3) test for alloy C done at 523–678 K at times varying between 0 and 24 h for different temperatures. Hardness data is averaged for XZ and XY directions and error bars of one standard deviation shown.

However since the volume fractions of the Al_3Zr phases are supposed to be low, it may not be detected. Furthermore, since the $Al_{12}Mn$ and Al_6Mn peaks are close for the 2Θ region of interest (38°–45°), it is hard to establish any direct correlation between amount of such precipitates. Fig. 6b) shows the peaks observed after ageing alloy C for 24 h at 648 K and 678 K. From the inset in the figure, it appears that the peak intensity for the Al-Mn precipitates is much stronger than after printing, and so in particular for ageing at 678 K. This suggests that the precipitates in question have increased in volume and that there is faster growth as the temperature is raised.

3.4. Optical microscopy

Optical microscopy was done on cross sections of alloy C in as-printed condition and overaged condition (648 K for 24 h). Etching was done using Keller's reagent. Fig. 7a) shows a typical image of as-printed sample of alloy C showing evidence of local grain refinement, which was observed at few locations only. It can be seen that there is precipitation at melt pool boundaries, seen as dark contrast. This is also shown to be the Al-Mn rich precipitates in coming sections. Fig. 7b) shows the typical appearance of the overaged condition for alloy C, for which the precipitates formed (Al-Mn base precipitates) are seen to be clearly decorating the grain boundaries in the microstructure.

3.5. Electron microscopy and EDX analysis

Electron microscopy was done on as-polished samples using back scattered detector, to study the compositional contrast between the precipitates and the matrix. Fig. 8 shows two representative areas before and after ageing of alloy C. For the as-printed condition (Fig. 8a)), small precipitates of the order < 100 nm are observed at grain boundaries and cell boundaries while some precipitates also occur at melt pool boundaries [24]. After ageing at 648 K for 8 h (Fig. 8b)), there is heavy precipitation of several types and size distributions, with the largest precipitates at grain boundaries. The grain boundary precipitates show two different contrasts referred to as "bright particle" and "dark particle". Based on EDX analysis (Fig. 8c)), it is suggested that the two different kinds of precipitates

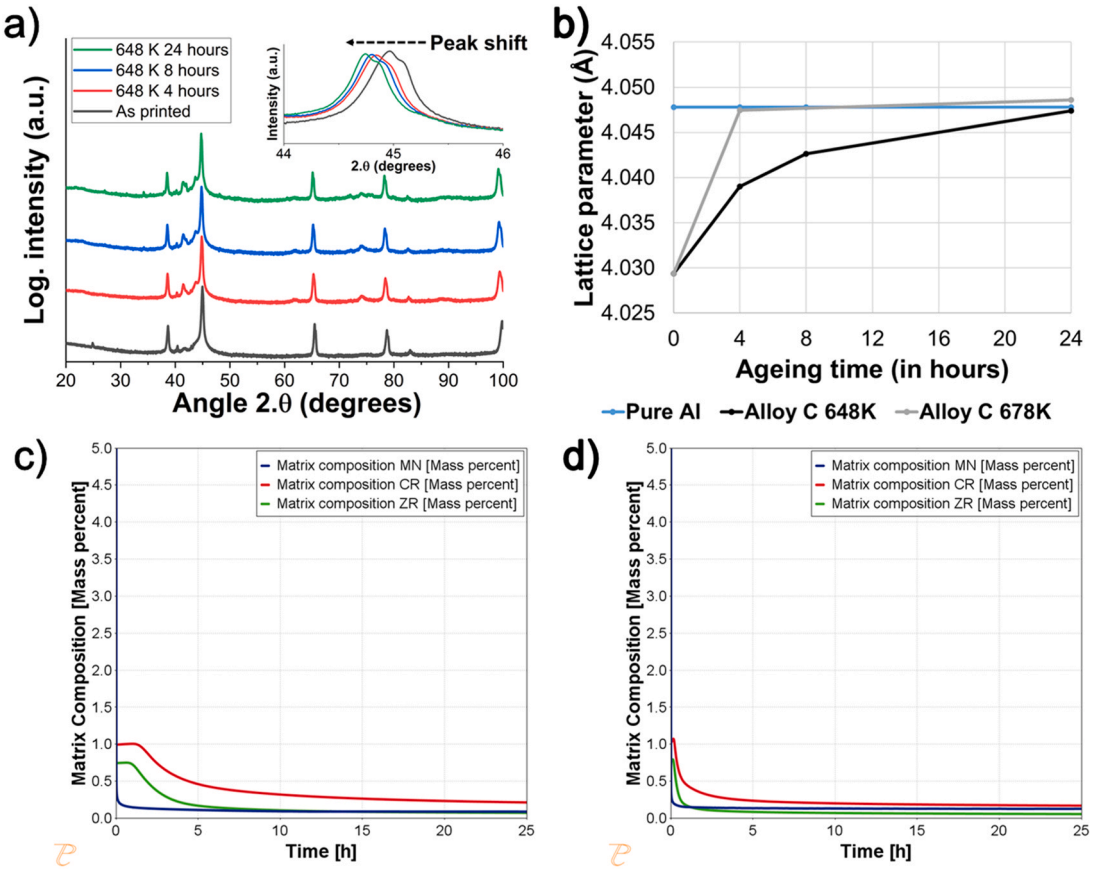

Fig. 5. a) X-ray diffractogram for Alloy C before and after ageing at 648 K. Peak shift in the Al-peak is observed b) Relative lattice parameter shift corresponding to this peak shift after heating at 648 K and 678 K c)-d) PRISMA calculations for Alloy C simulating the diffusion out of solutes at 648 K and 678 K respectively.

correspond to Al_6Mn and $Al_{12}Mn$ stoichiometries respectively. Another observation is that the region between these precipitates close to the grain boundary (marked in orange) was seen to contain only ~1 wt% Mn, showing localised depletion of Mn. The EBSD phase analysis, attached in supplementary data also suggests diffraction data corresponding to Al_6Mn and $Al_{12}Mn$ phases, using crystallographic information defined for the XRD analysis (shown in Table 3).

3.6. Al-Mn family of precipitates: feature analysis with EDX

Feature analysis was conducted by combining EDX point analysis and back scatter electron (BSE) imaging. This method enables high throughput image analysis by detecting precipitates as BSE grey contrast over a large total field of view stitched as a montage and then detect the precipitates with EDX point scans, thus opening up the possibility for quantitative analysis of precipitate sizes and chemistries in bulk samples, which is not possible with localised analysis such as TEM. Three scanned areas of 0.23 mm × 0.17 mm each were investigated for each of the heat-treated condition selected, thus in total ~0.12 mm^2 was scanned per sample. In this analysis, the precipitates were then classified based on the amount of Mn (wt%) detected for three sub-classes:

1. Matrix precipitates (< 5 wt% Mn): These could be shallow precipitates that could not be resolved due to depleted Al substrate below, thus diluting the pickup of Mn. They were used as indicators for precipitations only and not used for chemistry comparison.
2. $Al_{12}Mn$ precipitates (5–20 wt% Mn): These are possibly the semi-coherent $Al_{12}Mn$ precipitates. Since the matrix is expected to have 5 wt% Mn, a richer composition would indicate $Al_{12}Mn$ precipitate. However, small amount of Al_6Mn could be wrongly detected as $Al_{12}Mn$ (if precipitates are relatively small, thus substrate diluting the chemistry).
3. Al_6Mn precipitates (> 20 wt% Mn): These are expected to be the incoherent Al_6Mn precipitates formed on ageing in Mn-containing Al-alloys.

Table 3
Crystallographic parameters for the different phases seen in the alloys.

Phase	Crystal class	Space group	Symbol	Lattice parameters (Å)	Reference
Al	Cubic	$Fm\bar{3}m$	Δ	a = 4.047 Å	PDF nr. 0040787
Al_6Mn	Orthorhombic	Cmcm	◆	a = 7.55 Å b = 6.50 Å c = 8.87 Å	[26,27]
$Al_{12}Mn$	Cubic	$Im\bar{3}$	◊	a = 7.47 Å	[28]
Al_3Zr_L12	Cubic	Pm-3 m	○	a = 4.093 Å	PDF nr. 040012612
Al_3Zr_D023	Tetragonal	I4/mmm	●	a = 4.009 Å c = 17.281 Å	PDF nr. 000481385

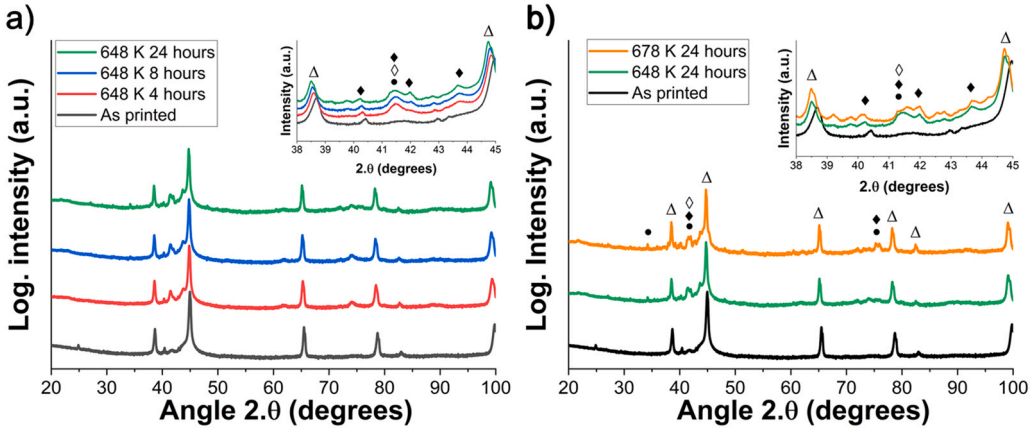

Fig. 6. a) X-ray diffractogram for Alloy C before and after ageing at 648 K. Minor peaks between 38° and 45° 2Θ values are shown in inset image. b) X-ray diffractogram for Alloy C overaged for 24 h at two different temperatures (648 K, 678 K). Minor peaks observed are shown in inset. The peaks are associated with Al_6Mn (♦), $Al_{12}Mn$ (◊), Al_3Zr (•).

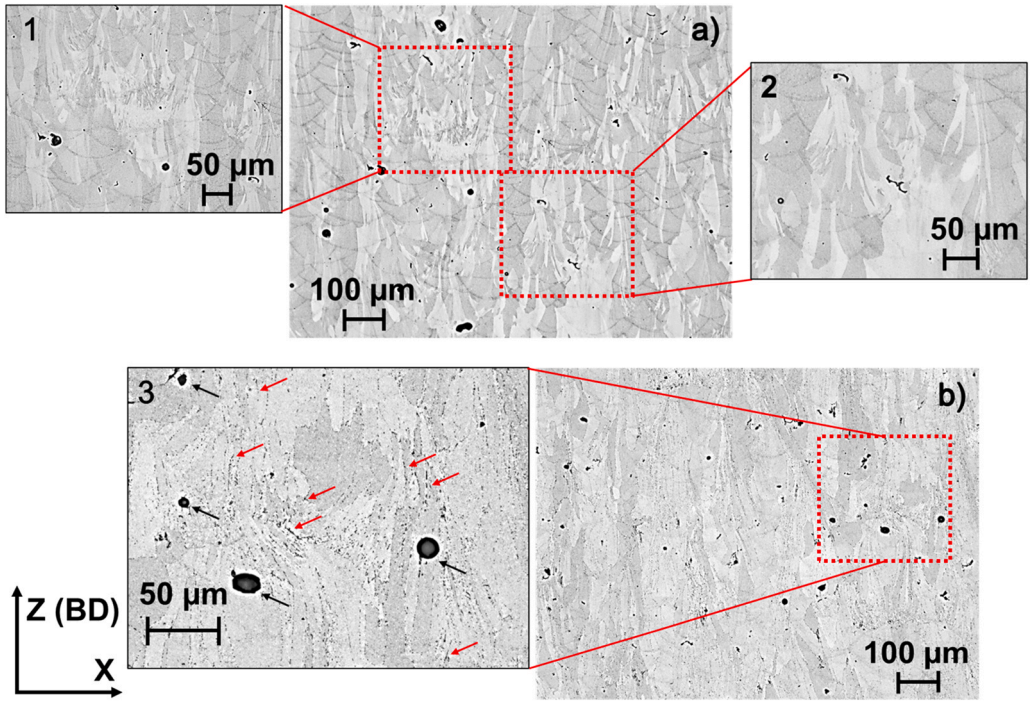

Fig. 7. Etched microstructure of alloy C in a) as-printed and b) overaged at 648 K 24 h condition at low magnifications. Two types of grain morphology regions illustrated in a) namely 1:refined grain region where grain sizes < 5 µm and 2: Columnar grain region where larger grains > 50–100 µm as illustrated in the inset of an overaged sample b), 3: grain boundary precipitates are marked in red and porosity is marked in black.

Fig. 9a-d shows one of the SEM images each (out of three each used for feature analysis) for alloy C samples before (as-printed condition; 0 h) and after ageing at 648 K for 8, 14 and 24 h respectively. These images were used for detection of the precipitates for feature analysis. A clear precipitation at grain boundaries is observed after initial ageing up to 8 h with mostly matrix precipitates or $Al_{12}Mn$ precipitates. After 14 h, Al_6Mn precipitates can be seen, and some bulk precipitation has started. On further ageing at 24 h precipitation mainly occurs in the bulk of the sample (inside grains) with several precipitates observed at melt pool boundaries. Fig. 8c), and Table 4 summarise the chemistry and morphology data from the feature analysis. The results are confirmed visually with help of the feature analysis in Fig. 9c)-d), in which a significantly high number of precipitates are detected. This observation is also backed up by depletion of grain boundary regions in Mn seen in grain boundary regions as illustrated in Fig. 8c).

Quantitative analysis of $Al_{12}Mn$ and Al_6Mn classes of precipitates was conducted only in the sample aged at 648 K. The matrix precipitates were ignored (sub class 1) to avoid possibility of noise detected as precipitates. It can be seen from Fig. 10 that the relative increase in amount of precipitates from as-printed (0 h) to 8 h of ageing (2000 → 29800) is only matched when comparing the amounts after 14 h and 24 h of ageing (35300 → 62500). Contrary to these observations, the increase in precipitates from 8 h to 14 h of ageing is smaller (29800 → 35300). Table 4 provides D50 and D90 (in µm) values for the precipitates shown in Fig. 10. More data can be found in supplementary section. It can be seen here that both the number and number fraction of Al_6Mn precipitates as compared to total precipitates increase with time; there is a change from about 5–12% of number of total precipitates from as-printed (0 h) and 24 h ageing at 648 K. Considering the equivalent circular diameter (ECD) data in Table 4, the ECD (in µm) for Al_6Mn precipitates changes over

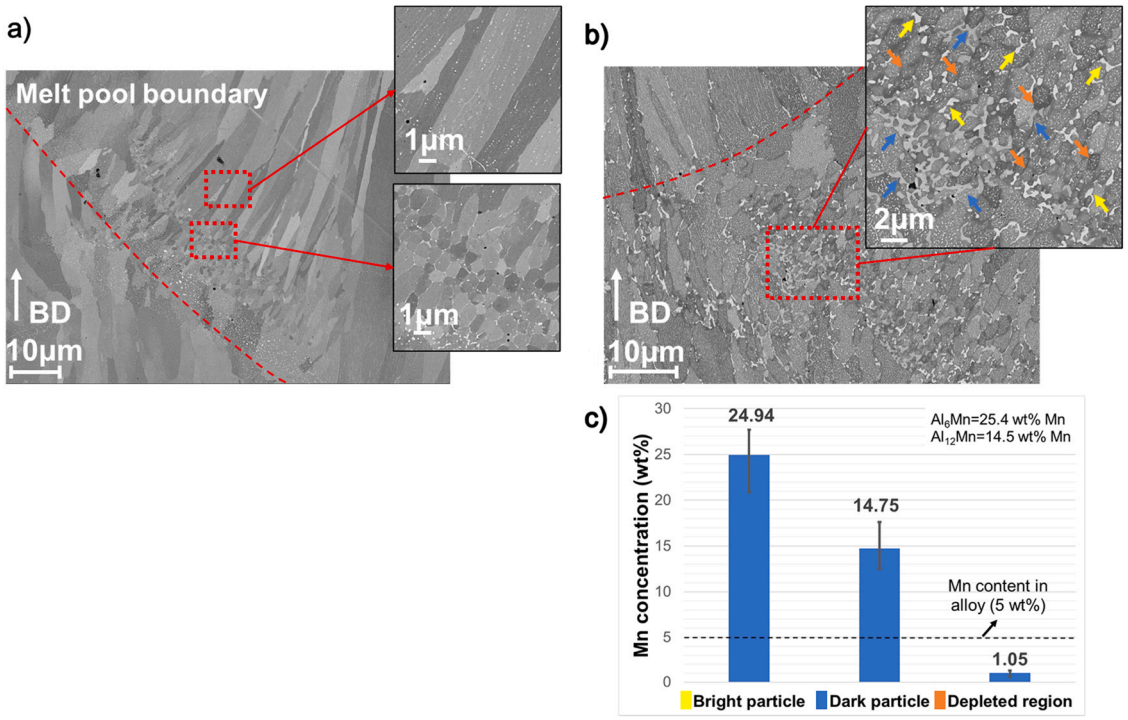

Fig. 8. a) SEM image for as-printed sample of alloy C showing difference in grain sizes for the regions where grain refinement occurs. Melt pool boundary is marked in red. b) SEM image for alloy C aged at 648 K 8 h showing heavy precipitation with largest precipitates at grain boundaries. The $Al_{12}Mn$ (darker contrast) precipitates are marked in blue whereas the Al_6Mn (brighter contrast) precipitates are marked in yellow. The regions between precipitates where Mn is depleted are shown in orange c) EDX point scan result for Mn content in the three different regions shown.

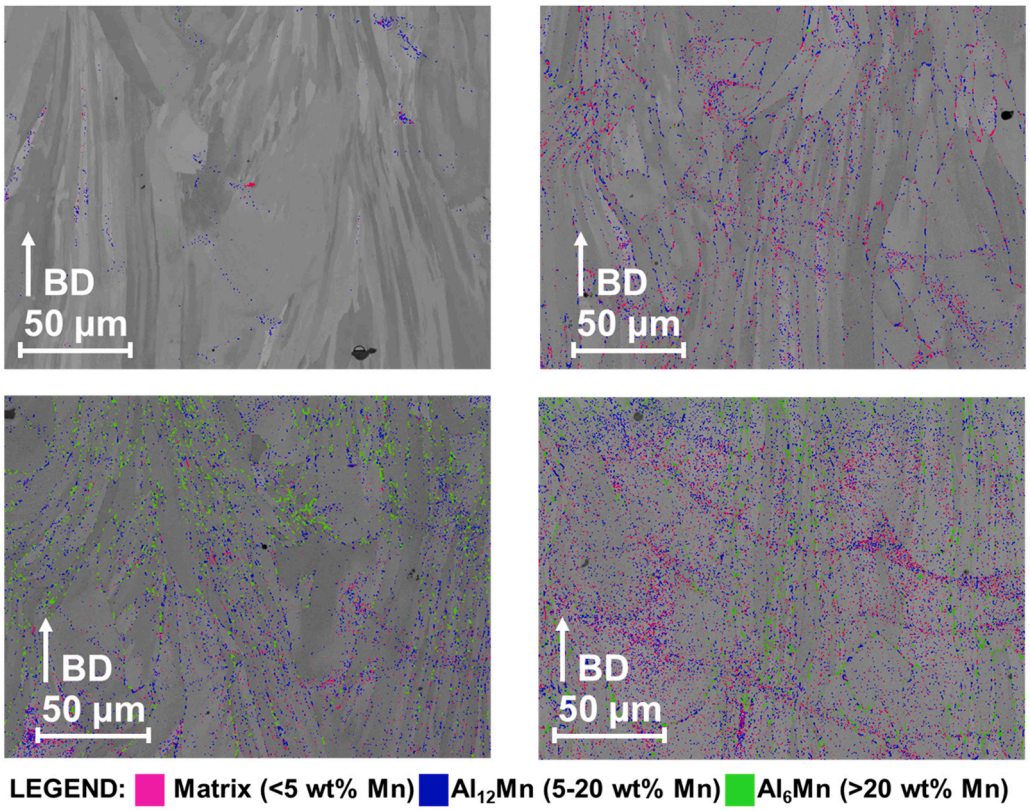

Fig. 9. SEM image with EDX feature analysis results for alloy C a) before and b)-d) after ageing at 648 K for 8, 14, 24 h respectively.

time (D90 values go from 0.499 μm to 0.759 μm between 0 and 24 h at 648 K). Possible reasons could be that smaller $Al_{12}Mn$ precipitates transform to Al_6Mn or existing Al_6Mn precipitates grow over time. The D90 value for $Al_{12}Mn$ precipitates increases between 0 and 8 h from 0.256 μm to 0.409 μm and then decreases slightly to 0.318 μm after 14 h. This value then reaches to 0.342 μm after further ageing

Table 4
Summary of values shown to reflect the D50 (50th percentile) and D90 (90th percentile) values of the ECD (in μm) for different precipitate classes at different ageing times.

Condition	Precipitate type	D50 (μm)	D90 (μm)
As-printed	$Al_{12}Mn$	0.177	0.256
	Al_6Mn	0.312	0.499
648 K 8 h	$Al_{12}Mn$	0.197	0.409
	Al_6Mn	0.364	0.739
648 K 14 h	$Al_{12}Mn$	0.187	0.318
	Al_6Mn	0.318	0.621
648 K 24 h	$Al_{12}Mn$	0.197	0.342
	Al_6Mn	0.380	0.759

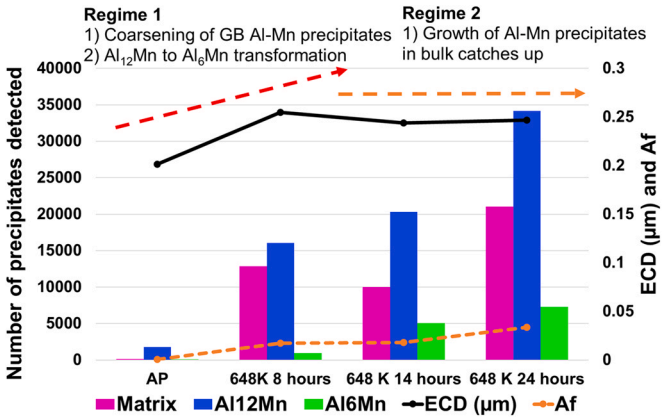

Fig. 10. Summary of feature analysis results. The number of matrix, $Al_{12}Mn$ and Al_6Mn precipitates detected as a fraction of total precipitates over different times is plotted on the primary Y axis. The equivalent circular diameter (ECD, in μm) and Area fraction (A_f) of the precipitates is plotted on the secondary Y axis.

between 14 and 24 h while the number of $Al_{12}Mn$ precipitates increases by ~70%; depicted by number count increase from 20300 to 34000 (Fig. 10). This indicates that a high number of new precipitates are formed between 14 and 24 h of ageing.

3.7. Al-Zr family of precipitates

A small amount of nanosized spherical Al-Zr precipitates are expected to be found in the bulk. These precipitates are well-documented and known for their high strengthening potential to the Zr-containing Al-alloys [12,29]. The precipitation of Al-Zr was characterised in Alloy C for all the four heat treated conditions namely 648 K for 0, 8, 14 and 24 h. As shown in Fig. 11 a)-b) the Al-Zr precipitates are co-precipitated with Al-Mn precipitates. This was observed for all three aged samples consistently (8, 14 and 24 h). The Al-Zr precipitates were seen together with several Al-Mn precipitates, both in the bulk and at grain boundaries. The reason for this phenomenon was not found from literature and further experiments and calculations are needed to fully understand this. Two different size fractions of Al-Zr precipitates were observed. There were clusters of several small precipitates of ~10 nm size and fewer large precipitates between 25 and 60 nm in samples aged between 8 and 24 h. The summary shown in Fig. 11c)shows that the larger precipitates grow larger on average over ageing time as explained by the classical Ostwald ripening [30,31].

Furthermore, to verify that the precipitates shown in Fig. 11 are Al-Zr based, electron transparent samples were tested in S-TEM to verify enrichment of Zr in the spherical precipitates, as summarised in Fig. 12. It can be seen that point 1 (EDX on the spherical precipitate) is high in Al, Zr whereas point 2 (vacuum) has no significant presence of elements.

4. Discussion

High performance aluminium alloys developed by leveraging the benefit of high matrix solubility need to be analysed from the beginning of the process to the final mechanical behaviour, to develop reliable understanding of such novel systems. Although it is expected that full dissolution should be possible during the rapid solidification as expected to prevail in PBF-LB and shown for Al-Mn-Cr and Al-Mn-Zr alloys [32–34], it is seen in reality that lesser amounts of supersaturations is achievable via PBF-LB. This can be explained in part by the remelting effect illustrated in Fig. 13. The figure illustrated how each layer sequentially is remelted several times and thus a heat affected zone is developed below each deposited/ remelted layer, causing precipitation of secondary phase precipitates from supersaturated solid solution below [35,36]. These possible precipitates have been explained with the phase equilibrium temperature profile plots shown in Fig. 2. It is expected that they could be Al_6Mn or $Al_{12}Mn$ precipitates. This was verified for as-printed samples wherein XRD indicated formation of very small amount (< 5 vol%) of Al-Mn containing precipitates, which was further confirmed by means of electron microscopy[24]. The Al-Zr based, or Al-Fe based precipitates were not seen by either microscopy or XRD and thus, they were assumed to be completely dissolved during printing.

For high strength applications a heat treatment is required. Direct ageing was shown to be a better choice than typical T6 type heat treatment due to an extended non-equilibrium solubility achievable, which would be lost if solutioning treatment was conducted [2,37,38]. Figs. 3 and 4 confirm the strong hardening response in these alloys, especially alloy C which hardens by ~40% to reach 143 HV after ageing at 623 K for 24 h or 142 HV after ageing at 648 K for 14 h.

By linking the hardening results to the detailed microstructure analysis conducted in form of feature analysis as presented in Fig. 14, it can be said that the precipitation kinetics of Al-Mn-Cr-Zr containing alloys is complex. The primary hardening precipitate is Al-Zr based. For the Al-Mn based precipitates, there is a difference in precipitate growth rates depending on their location be it bulk or grain boundaries. Clearly the Al-Mn precipitates contribute to the hardening response, as seen for alloy B in Fig. 3. The hardening results when compared between alloy A and alloy C in Fig. 3 show a clear benefit of Cr in terms of both increasing as-printed hardness and improvement in peak hardening response. It is suggested that Cr helps to stabilise the hardening $Al_{12}Mn$ precipitate, forming the G-phase or $Al_{12}(Mn,Cr)$ [32,39]. It was hard to quantify the exact amount of Cr in Al-Mn precipitates yet as the chemical analysis was conducted on Lα lines, which have lower energy and are close for Mn, Cr ($Mn_{L\alpha1}$= 637 eV, Cr $_{L\alpha1}$= 572 eV). This elemental discrimination is currently being studied to identify Cr solubility in Al-Mn precipitates. The simulation of Cr solubility in Al-Mn precipitates is also not possible currently as commercial thermodynamic databases did not contain Cr as a possible element in Al-Mn precipitates. Fe on the other hand stabilises Al_6Mn (simulations shown in supplementary material) as the Al-Mn-Fe ternary is a system of interest in several commercial Al-alloys. Thus, it is used as an illustration to effect of stabilising elements to Al-Mn precipitates. Experimental results have also been reported by addition of tungsten (W) to Al-Mn containing materials to stabilise $Al_{12}Mn$ precipitates [40]. Chromium is one of the slowest diffusing element in Al-matrix [41] and adding Cr seems to cause more controlled hardening response.

The key to getting a good hardening response is to get a high volume fraction of coherent precipitates that harden the matrix by shear hardening (as in case of Al-Zr precipitates [42–44]). Alternatively, smaller radius of semi-coherent precipitates with high volume fraction can provide strong hardening as precipitates trigger the Orowan looping mechanism (in case of Al-Mn precipitates) [37,45]. Although the precipitation at grain boundaries is the

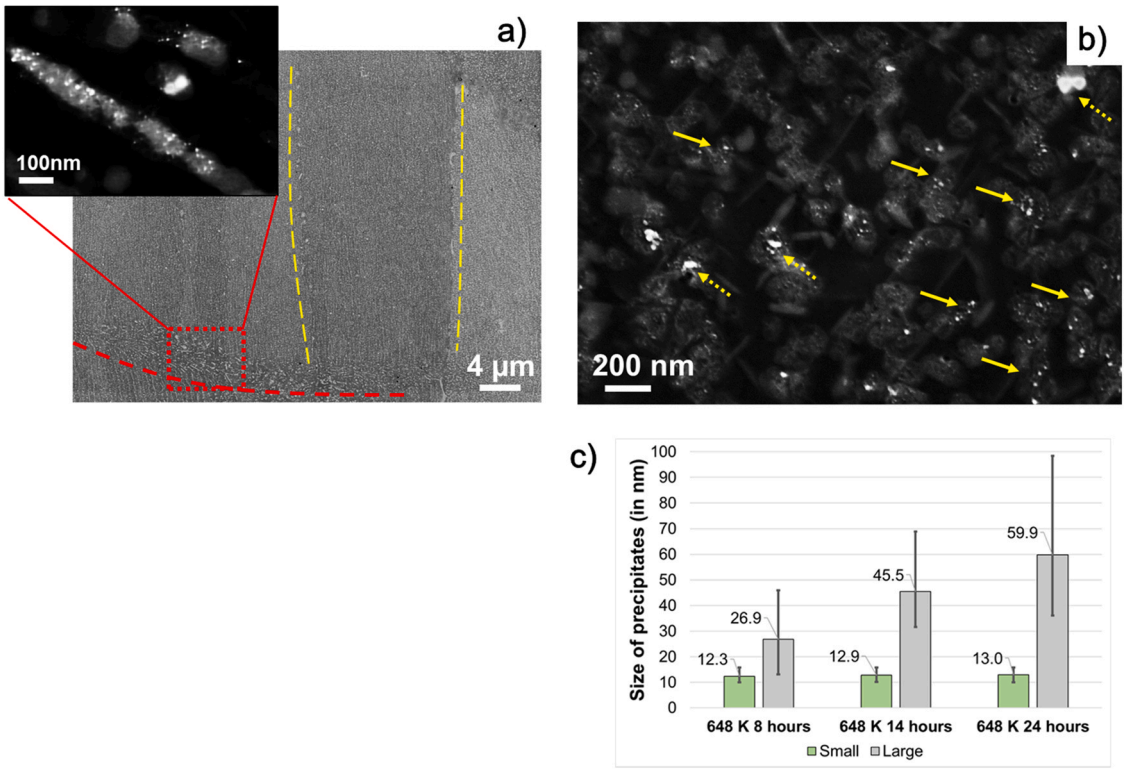

Fig. 11. a)-b) Al-Zr precipitates as seen in Alloy C aged at 648 K for 8 h a) Shows Al-Zr precipitates formed as clusters on Al-Mn precipitates and b) shows that Al-Zr precipitates have few large and several small precipitates exemplifying Ostwald ripening c) Average size of the large and small precipitates during 8, 14 and 24 h ageing at 648 K.

dominant region for growth of Al-Mn precipitates during initial heat treatments, it is suggested that this rate of precipitate growth slows down due to consumption of Mn available around grain boundaries, demarcated by depleted regions illustrated in Fig. 8, reaching within a certain period of time equilibrium solubility of Mn in Al (around 1 wt%). As a consequence, significant Al-Mn precipitate growth in bulk is observed during microstructural characterization. These smaller precipitates in the bulk are suggested to contribute to a secondary peak hardening response illustrated in Fig. 14. The bulk Al-Mn precipitates seem also to directly affect the precipitation of the Al-Zr precipitates, the latter which were found to co-precipitate with Al-Mn precipitates, as confirmed from Fig. 11. This means that

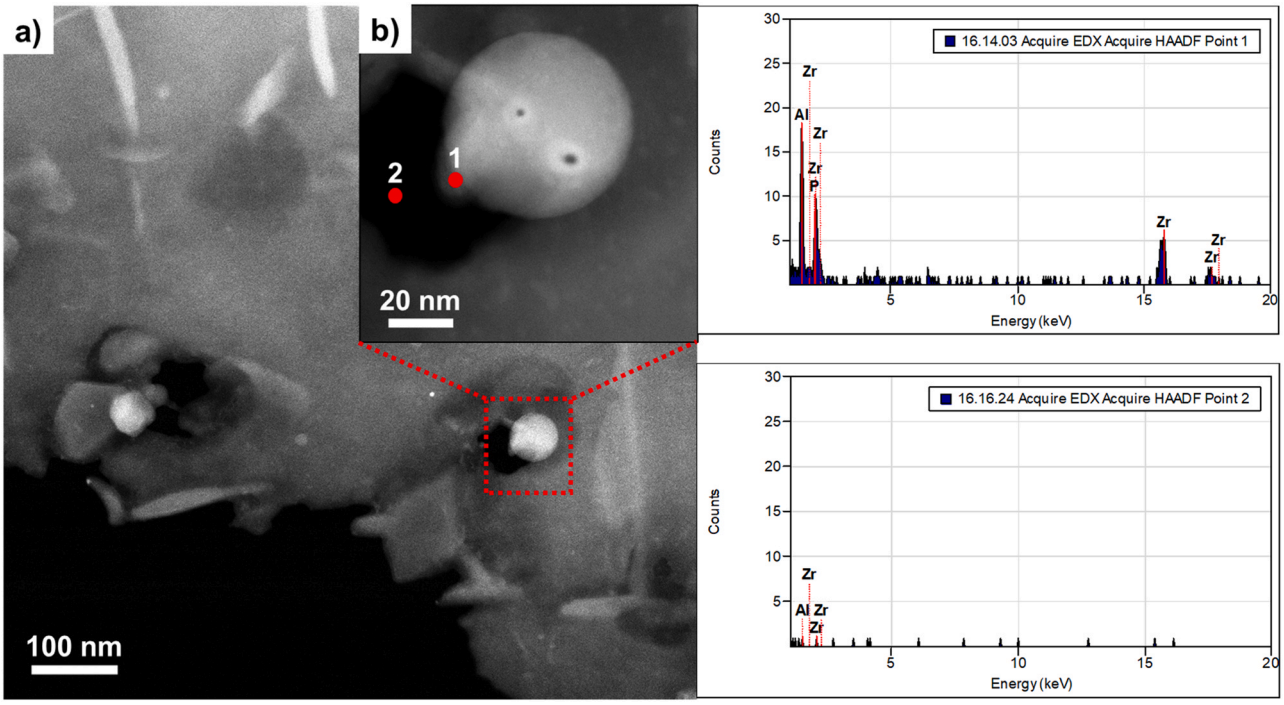

Fig. 12. a) STEM imaging done on Titan 80–300 TEM, confirming the Al-Zr precipitates in sample from alloy C aged at 648 K for 8 h b) Magnified image of one of the Al-Zr precipitate, which was confirmed using EDX chemical point scan (point 1) to reveal Zr enrichment as compared to vacuum (point 2).

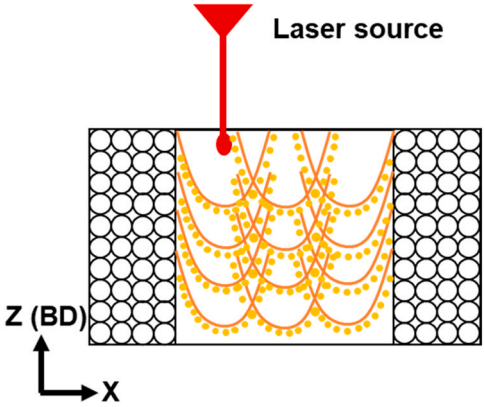

Fig. 13. Schematic of PBF-LB processing showing the precipitation that is seen to occur during printing of Al-Mn alloys. It is suggested that Mn rich precipitates form due to a supersaturation of the region below the re-melted zone.

the secondary peak hardening observed for ageing at 648 K could be a combined effect of Mn-containing and Zr-containing precipitates in the bulk. Similar two-stage hardening has been observed for rapidly solidified Al-Mn-Zr alloys on direct ageing at similar temperatures [33]. The authors in that study attributed the secondary peak from needle shaped Al-Mn precipitates isomorphous to Al_6Mn and did not mention any effect of nanoscale Al-Zr precipitates that as now well-established as precipitation strengthening contribution [29,42,43].

The explanation for the presence of larger precipitates at grain boundaries is proposed to be due to a faster diffusion at grain boundaries. As shown in previous study by the authors, small nanoscale precipitates were present at grain boundaries, cell boundaries and melt pool boundaries after PBF-LB processing [24]. However, among these it is only the grain boundary precipitates that grow significantly larger. Disregarding diffusion path width, the absolute diffusivity at grain boundaries is expected to be about five orders of magnitude faster than in the bulk at 650 K (Fig. 15).

The predictions using PRISMA calculations for this Al-alloy system studied appears to compare well with the interpretation of residual solute content from XRD peak positions as seen in Fig. 5. Finally, the application for this alloy is targeted towards high

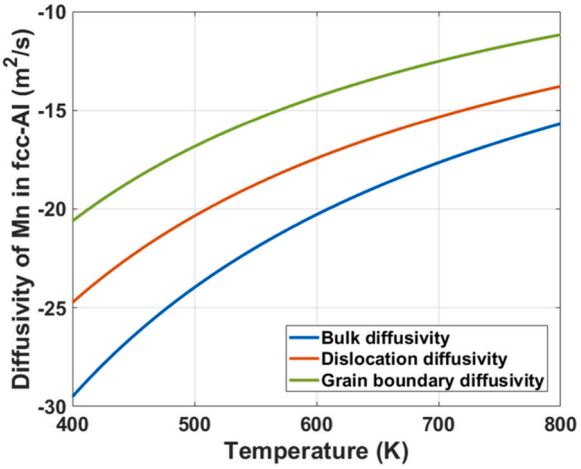

Fig. 15. Diffusivities of Mn in different regions in fcc-Al between 400 and 800 K temperature range. It can be seen clearly how grain boundary diffusion is higher by several orders of magnitude to bulk diffusion at 648 K. Curves based on [41,46,47].

temperature strengths [3], which is suggested by negligible hardening below 573 K and controlled precipitation hardening at 623–648 K as suggested in Fig. 4. The current set of experiments successfully indicate that. It can be summarised as follows.

1. The use of Mn, Cr, Zr as possible alloying elements was done based on theoretical data suggesting higher supersaturations with rapid solidification. [29,32,33,43,48,49].
2. Experimental hardening curves conclude that these alloys have slow precipitation kinetics and precipitation reactions that are seen to lead to high hardening effects (143 HV in case of alloy C).
3. Moreover, the alloys have shown considerable stability at these hardening temperatures; as seen for alloy C having 102 HV as-printed, 142 HV 14 h and 122 HV 100 h ageing at 648 K.

These observations combined with extensive microstructure analysis suggests that the strength is derived mostly from Al-Zr precipitates combined with a contribution from Al-Mn containing precipitates. Additionally, the Al-Zr precipitates are seen to co-precipitate with the Al-Mn precipitates making their precipitation

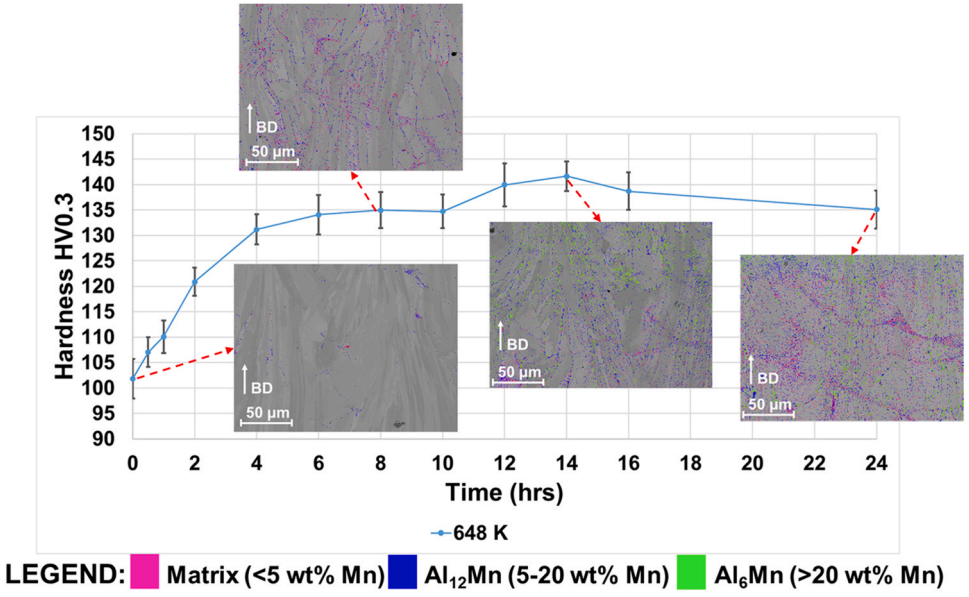

Fig. 14. Summary of precipitation kinetics due to Al-Mn precipitates in Alloy C during ageing at 648 K.

kinetics interlinked in some way. This means that the role of Al-Mn precipitates could be larger than simply hardening of the Al-matrix.

5. Conclusions

Precipitation kinetics in novel Al-Mn-Cr-Zr based alloys tailored for PBF-LB process have been studied. These alloys have a high supersaturation of solutes namely Mn, Cr and Zr in the as-printed state owing to high solidification rates in the PBF-LB process. This enables a strong hardening response upon direct ageing, with about 40% increase in hardness in one of the alloys. Some of the aforementioned samples were further analysed using X-ray diffraction, electron microscopy and coupled with thermodynamic simulations to understand how the precipitation behaviour can be explained. It was seen that two families of precipitates namely Al-Mn containing and Al-Zr containing precipitates are formed. The Al-Mn precipitates are seen to have faster growth at grain boundaries in beginning of heat treatments, followed by bulk precipitation growth. It is further shown that these precipitates provide minor hardening to the bulk as well. The Al-Zr precipitates are the major contributor to hardness increase in the material. Interestingly, these precipitates are seen to be found to co-precipitate with Al-Mn containing precipitates, thus suggesting an interlinked precipitation reaction. Lastly, the addition of Cr in the alloys is seen to considerably improve the precipitation behaviour by a possible retardation of Al-Mn containing precipitate growth and thus forming a more pronounced hardening curve achieving 142–143 HV hardness for one of the alloys.

CRediT authorship contribution statement

Bharat Mehta: Conceptualization, Methodology, Investigation, Writing – original draft, Project administration **Karin Frisk:** Conceptualization, Methodology, Investigation, Data curation, Writing – review & editing, Supervision **Lars Nyborg:** Conceptualization, Methodology, Data curation, Funding acquisition, Writing – review & editing, Supervision.

Declaration of Competing Interest

The authors declare that they have no known competing financial interests or personal relationships that could have appeared to influence the work reported in this paper.

Acknowledgements

The authors would like to acknowledge the funding from Strategic Innovation Programme LIGHTer with support from VINNOVA, FORMAS and Energimyndigheten. In the current case specific funding is allocated via VINNOVA grant number 2018–02844 to the project ALL-Light. Centre of Additive Manufacturng-Metal (CAM2) hosted by Chalmers University of Technology which is sponsored via VINNOVA grant number 2016–05175 is also acknowledged and Production Area of Advance at Chalmers University. Authors are grateful to Adj. Prof. Sven Bengtsson and Sigurd Berg at Höganäs AB for help providing the powder and involvement in alloy designing discussions. Prof. Uta Klement is acknowledged for good discussions that helped plan the microscopy experiments better. Yiming Yao at Industrial and Materials Science department at Chalmers University is acknowledged for helping with EBSD result validation and discussions. Björn Skårman at Höganäs AB is acknowledged for conducting X-ray diffraction experiments and their interpretations. Dmitri Riabov and Tea Bertilsson at Höganäs AB are acknowledged for help with conducting ICP-AES analysis. Ludvig De Knoop at Chalmers Materials and Analysis Laboratory (CMAL) hosted by Physics Department, Chalmers University is acknowledged for conducting the TEM experiments. Andreas Markström and ThermoCalc AB are acknowledged for providing the latest software and fruitful discussions.

Declaration of interests

There is no conflict of interest from the authors.

Appendix A. Supporting information

Supplementary data associated with this article can be found in the online version at doi:10.1016/j.jallcom.2022.165870.

References

[1] G.E. Totten, D.S. Mackenzie, Principles of heat treating of nonferrous alloys *, vol. 4, (2016), https://doi.org/10.31399/asm.hb.v04e.a0006250
[2] T.H.E. Major, A. Alloy, Heat treatment practices of age-hardenable aluminum alloys *, vol. 4, (c) (2016), https://doi.org/10.31399/asm.hb.v04e.a0006288
[3] R.A. Michi, A. Plotkowski, A. Shyam, R.R. Dehoff, S.S. Babu, Towards high-temperature applications of aluminium alloys enabled by additive manufacturing, Int. Mater. Rev. (2021), https://doi.org/10.1080/09506608.2021.1951580
[4] O.D. Krainikov, A.V. Neikov, Sintered metals and alloys rapidly solidified high-temperature aluminum, Powder Metall. Met. Ceram. vol. 51, (9) (2013) 554–565.
[5] T. DebRoy, et al., Additive manufacturing of metallic components – process, structure and properties, Prog. Mater. Sci. vol. 92, (2018) 112–224, https://doi.org/10.1016/j.pmatsci.2017.10.001
[6] W.E. Frazier, Metal additive manufacturing: a review, J. Mater. Eng. Perform. vol. 23, (6) (2014) 1917–1928, https://doi.org/10.1007/s11665-014-0958-z
[7] N. Guo, M.C. Leu, Additive manufacturing: technology, applications and research needs, Front. Mech. Eng. vol. 8, (3) (2013) 215–243, https://doi.org/10.1007/s11465-013-0248-8
[8] A. Leicht, Laser powder bed fusion of 316L stainless steel Microstructure and mechanical properties as a function of process. 2020.
[9] D.D. Gu, W. Meiners, K. Wissenbach, R. Poprawe, Laser additive manufacturing of metallic components: Materials, processes and mechanisms, Int. Mater. Rev. vol. 57, (3) (2012) 133–164, https://doi.org/10.1179/1743280411Y.0000000014
[10] N.T. Aboulkhair, M. Simonelli, L. Parry, I. Ashcroft, C. Tuck, R. Hague, 3D printing of aluminium alloys: additive manufacturing of aluminium alloys using selective laser melting, Prog. Mater. Sci. vol. 106, (August 2018) (2019) 100578, https://doi.org/10.1016/j.pmatsci.2019.100578
[11] J.H. Martin, B.D. Yahata, J.M. Hundley, J.A. Mayer, T.A. Schaedler, T.M. Pollock, 3D printing of high-strength aluminium alloys, Nature vol. 549, (7672) (2017) 365–369, https://doi.org/10.1038/nature23894
[12] J.R. Croteau, et al., Microstructure and mechanical properties of Al-Mg-Zr alloys processed by selective laser melting, Acta Mater. vol. 153, (2018) 35–44, https://doi.org/10.1016/j.actamat.2018.04.053
[13] Q. Jia, et al., Selective laser melting of a high strength Al[sbnd]Mn[sbnd]Sc alloy: alloy design and strengthening mechanisms, Acta Mater. vol. 171, (2019) 108–118, https://doi.org/10.1016/j.actamat.2019.04.014
[14] K. Schmidtke, F. Palm, A. Hawkins, and C. Emmelmann, Process and mechanical properties: Applicability of a scandium modified Al-alloy for laser additive manufacturing, 2011. doi:10.1016/j.phpro.2011.03.047.
[15] L. Zheng, Y. Liu, S. Sun, H. Zhang, Selective laser melting of Al-8.5Fe-1.3V-1.7Si alloy: investigation on the resultant microstructure and hardness, Chin. J. Aeronaut. (2015), https://doi.org/10.1016/j.cja.2015.01.013
[16] S. Thapliyal, et al., An integrated computational materials engineering-anchored closed-loop method for design of aluminum alloys for additive manufacturing, Mater. (Oxf.) vol. 9, (December 2019) (2020) 100574, https://doi.org/10.1016/j.mtla.2019.100574
[17] H. Jones, "Development in aluminium alloys by solidification at higher cooling rates," Sheffield, UK, 1978.
[18] P. Furrer, H. Warlimont, Gefüge und Eigenschaften von Aluminiumlegierungen nach rascher Erstarrung, Int. J. Mater. Res. vol. 62, (2) (1971) 100–112, https://doi.org/10.1515/ijmr-1971-620204
[19] S. Kou, A criterion for cracking during solidification, Acta Mater. vol. 88, (2015) 366–374, https://doi.org/10.1016/j.actamat.2015.01.034
[20] K. Schmidtke, F. Palm, A. Hawkins, C. Emmelmann, Process and mechanical properties: Applicability of a scandium modified Al-alloy for laser additive manufacturing, Phys. Procedia vol. 12, (PART 1) (2011) 369–374, https://doi.org/10.1016/j.phpro.2011.03.047
[21] A. Mehta, et al., Additive manufacturing and mechanical properties of the dense and crack free Zr-modified aluminum alloy 6061 fabricated by the laser-powder bed fusion, Addit. Manuf. vol. 41, (November 2020) (2021) 101966, https://doi.org/10.1016/j.addma.2021.101966
[22] J. Fiocchi, A. Tuissi, C.A. Biffi, Heat treatment of aluminium alloys produced by laser powder bed fusion: a review, Mater. Des. vol. 204, (2021), https://doi.org/10.1016/j.matdes.2021.109651
[23] L. Thijs, K. Kempen, J.P. Kruth, J. van Humbeeck, Fine-structured aluminium products with controllable texture by selective laser melting of pre-alloyed

AlSi10Mg powder, Acta Mater. vol. 61, (5) (2013) 1809–1819, https://doi.org/10.1016/j.actamat.2012.11.052
[24] B. Mehta, L. Nyborg, K. Frisk, E. Hryha, Al–Mn–Cr–Zr-based alloys tailored for powder bed fusion-laser beam process: alloy design, printability, resulting microstructure and alloy properties, J. Mater. Res. vol. 3, (2022) 1–13, https://doi.org/10.1557/s43578-022-00533-1
[25] I. Ansara, A.T. Dinsdale, M.H. Rand, Thermochemical database for light metal alloys, vol. 2. 1998.
[26] M.A. Gordillo, I. Cernatescu, T.T. Aindow, T.J. Watson, and M. Aindow, Phase stability in a powder-processed Al – Mn – Ce alloy, pp. 3742–3754, 2014, doi:10.1007/s10853–014-8086–6.
[27] A.D.I. Nicol, The structure of MnAl6, Acta Cryst. vol. 6, (1953) 285–293, https://doi.org/10.2320/matertrans1960.15.185
[28] J. Adam, J.B. Rich, The crystal structure of WAl 12, MoAl 12 and (Mn, Cr)Al 12, Acta Crystallogr. vol. 7, (12) (1954) 813–816, https://doi.org/10.1107/s0365110×54002514
[29] K.E. Knipling, D.C. Dunand, D.N. Seidman, Precipitation evolution in Al-Zr and Al-Zr-Ti alloys during aging at 450–600 °C, Acta Mater. vol. 56, (6) (2008) 1182–1195, https://doi.org/10.1016/j.actamat.2007.11.011
[30] V.C. Wagner, Theorie der Alterung Theorie der Alterung von Niederschliigen durch Umlosen (Ostwald-Reifung), Z. für Elektrochem., Ber. der Bunsenges. für Phys. Chem. vol. 65, (7–8) (1961) 581–591.
[31] E.A. Marquis, D.N. Seidman, Nanoscale structural evolution of Al3Sc precipitates in Al(Sc) alloys, Acta Mater. vol. 49, (11) (2001) 1909–1919, https://doi.org/10.1016/S1359-6454(01)00116-1
[32] P. Liu, G.L. Dunlop, L. Arnberg, Microstructural development in a rapidly solidified Al5Mn2.5Cr alloy, Mater. Sci. Eng. vol. 98, (C) (1988) 437–441, https://doi.org/10.1016/0025-5416(88)90202-9
[33] T. Ohashi, L. Dai, N. Fukatsu, Decomposition characteristics of al-mn-zr alloys rapidly-quenched from the melt, Metall. Trans. A, Phys. Metall. Mater. Sci. vol. 17, (5) (1986) 799–806, https://doi.org/10.1007/BF02643855
[34] H. Jones, Chapter 3 Rapid solidification, Pergamon Mater. Ser. vol. 2, (C) (1999) 23–45, https://doi.org/10.1016/S1470-1804(99)80049-2
[35] P. Kürnsteiner, et al., Control of thermally stable core-shell nano-precipitates in additively manufactured Al-Sc-Zr alloys, Addit. Manuf. vol. 32, (September 2019) (2020) 100910, https://doi.org/10.1016/j.addma.2019.100910
[36] W. Hearn, “Laser based powder bed fusion of plain carbon and low-alloy steels: microstructure and processability,” p. 54, 2021, [Online]. Available: https://research.chalmers.se/en/publication/522034%0Ahttps://research.chalmers.se/publication/522034/file/522034_Fulltext.pdf.
[37] B. MEHTA, “High Performance Aluminium Alloys for Laser Powder Bed Fusion: Alloy Design and Development,” p. 48, 2021, [Online]. Available: https://www.chalmers.se/sv/institutioner/ims/kalendarium/Sidor/High-Performance-Aluminium-Alloys-for-Laser-Powder.aspx%0Ahttps://research.chalmers.se/publication/527075/file/527075_Fulltext.pdf.
[38] N.T. Aboulkhair, M. Simonelli, L. Parry, I. Ashcroft, C. Tuck, R. Hague, 3D printing of Aluminium alloys: Additive Manufacturing of Aluminium alloys using selective laser melting, Prog. Mater. Sci. (2019), https://doi.org/10.1016/j.pmatsci.2019.100578
[39] L.F. Mondolfo, Al–Cr–Mn aluminum–chromium–manganese system, Alum. Alloy. vol. 12, (1976) 483–485, https://doi.org/10.1016/b978-0-408-70932-3.50188-1
[40] Y. Fan, M.M. Makhlouf, Stabilizing the strengthening precipitates in aluminum-manganese alloys by the addition of tungsten, Mater. Sci. Eng. A vol. 691, (March) (2017) 1–7, https://doi.org/10.1016/j.msea.2017.03.025
[41] Y. Du, et al., Diffusion coefficients of some solutes in fcc and liquid Al: critical evaluation and correlation, Mater. Sci. Eng. A (2003), https://doi.org/10.1016/S0921-5093(03)00624-5
[42] D.N. Seidman, E.A. Marquis, D.C. Dunand, Precipitation strengthening at ambient and elevated temperatures of heat-treatable Al(Sc) alloys, Acta Mater. vol. 50, (16) (2002) 4021–4035, https://doi.org/10.1016/S1359-6454(02)00201-X
[43] K.E. Knipling, D.C. Dunand, D.N. Seidman, Criteria for developing castable, creep-resistant aluminum-based alloys - a review, Int. J. Mater. Res. vol. 97, (3) (2006) 246–265.
[44] K.E. Knipling, D.N. Seidman, D.C. Dunand, Ambient- and high-temperature mechanical properties of isochronally aged Al-0.06Sc, Al-0.06Zr and Al-0.06Sc-0.06Zr (at%) alloys, Acta Mater. vol. 59, (3) (2011) 943–954, https://doi.org/10.1016/j.actamat.2010.10.017
[45] R.O. Scattergood, D.J. Bacon, The Orowan mechanism in anisotropic crystals, Philos. Mag. vol. 31, (1) (1975) 179–198, https://doi.org/10.1080/14786437508229295
[46] J. Svoboda, F.D. Fischer, P. Fratzl, E. Kozeschnik, Modelling of kinetics in multi-component multi-phase systems with spherical precipitates I: Theory, Mater. Sci. Eng. A vol. 385, (1–2) (2004) 166–174, https://doi.org/10.1016/j.msea.2004.06.018
[47] E. Kozeschnik, J. Svoboda, R. Radis, F.D. Fischer, Mean-field model for the growth and coarsening of stoichiometric precipitates at grain boundaries, Model. Simul. Mater. Sci. Eng. vol. 18, (1) (2010), https://doi.org/10.1088/0965-0393/18/1/015011
[48] T. Uesugi, K. Higashi, First-principles studies on lattice constants and local lattice distortions in solid solution aluminum alloys, Comput. Mater. Sci. vol. 67, (2013) 1–10, https://doi.org/10.1016/j.commatsci.2012.08.037
[49] T. Uesugi and K. Higashi, Modeling Solid Solution Strengthening Using First-Principles Results of Misfit Strain with Friedel Model in Al-Based Alloys, pp. 1421–1425, 2010.